A self-filling microfluidic device for noninvasive and time-resolved single red blood cell experiments

Michael Göllner, Adriana C. Toma, Natalja Strelnikova, Siddharth Deshpande, and Thomas Pfohl

Citation: Biomicrofluidics **10**, 054121 (2016); doi: 10.1063/1.4966212
View online: http://dx.doi.org/10.1063/1.4966212
View Table of Contents: http://scitation.aip.org/content/aip/journal/bmf/10/5?ver=pdfcov
Published by the AIP Publishing

BIOMICROFLUIDICS **10**, 054121 (2016)

A self-filling microfluidic device for noninvasive and time-resolved single red blood cell experiments

Michael Göllner, Adriana C. Toma, Natalja Strelnikova, Siddharth Deshpande,[a] and Thomas Pfohl[b]
Department of Chemistry, University of Basel, 4056 Basel, Switzerland

(Received 16 August 2016; accepted 14 October 2016; published online 25 October 2016)

Existing approaches to red blood cell (RBC) experiments on the single-cell level usually rely on chemical or physical manipulations that often cause difficulties with preserving the RBC's integrity in a controlled microenvironment. Here, we introduce a straightforward, self-filling microfluidic device that autonomously separates and isolates single RBCs directly from unprocessed human blood samples and confines them in diffusion-controlled microchambers by solely exploiting their unique intrinsic properties. We were able to study the photo-induced oxygenation cycle of single functional RBCs by Raman microscopy without the limitations typically observed in optical tweezers based methods. Using bright-field microscopy, our noninvasive approach further enabled the time-resolved analysis of RBC flickering during the reversible shape evolution from the discocyte to the echinocyte morphology. Due to its specialized geometry, our device is particularly suited for studying the temporal behavior of single RBCs under precise control of their environment that will provide important insights into the RBC's biomedical and biophysical properties. *Published by AIP Publishing*. [http://dx.doi.org/10.1063/1.4966212]

INTRODUCTION

The red blood cell is the most abundant cell type in the human body and one in six humans in the world is affected by red blood cell (RBC) abnormalities, which are both a cause of and a biomarker for diseases.[1,2] In particular, the anucleate RBC is unique among human cell types as it presents a remarkable capability to undergo large passive deformations in order to traverse narrow micro-capillaries with cross-sections as small as one-third of its own diameter. Single-cell analysis became increasingly important[3] and revealed that the RBC's unique deformability is the combined result of the elastic properties of the membrane-cytoskeleton complex, the surface area-to-volume ratio, and the viscosity determined by the hemoglobin content.[4] Especially, the vibratory motions of the RBC's plasma membrane, referred to as "flickering,"[5] have been related to its biomechanical properties, which have been studied extensively in both single-cell experiments and theoretical work.[6–10] Moreover, the membrane fluctuations may also control adhesive phenomena, such as rouleau formation.[8] The presence of rouleaux is a cause of blood-related disorders and there are many pathological cases like malaria or sickle cell anemia where RBCs form these large aggregates that hinder blood flow.[11] Due to the severely altered biomechanical properties of malaria-infected RBCs during the disease progress, flickering analysis additionally shows promising potential for malaria diagnosis.[12]

The overall morphology of the RBC is another diagnostic indicator that is encoded in the mechanical properties of the cell membrane, and microfluidics with its unique advantages has been successfully used to investigate the sickling of RBCs associated with sickle cell anemia.[13] Furthermore, several theoretical studies predicted the morphological transition from the normal

[a]Present address: Department of Bionanoscience, Delft University of Technology, 2628 CJ Delft, The Netherlands.
[b]Present address: Biomaterials Science Center (BMC), University of Basel, 4123 Allschwil, Switzerland. Electronic mail: thomas.pfohl69@gmail.com.

discocyte to a series of crenated echinocyte shapes that appear under certain conditions like increasing salt concentration or adenosine triphosphate (ATP) depletion.[14–16] As an alternative to standard optical methods, Raman microscopy has emerged as a powerful technique to investigate not only the mechanical properties but also the molecular processes within single RBCs.[17–21] So-called Raman tweezers, which is the coupling of Raman spectroscopy with optical tweezers, have been successfully used to distinguish between healthy and diseased cells in thalassemia.[21,22]

All approaches to single-cell experiments are based on the same principle, the combination of a method to separate and isolate individual cells from the bulk with a technique to extract the relevant biological or biophysical information. Ideally, the principle that enables separation and isolation should apply minimal stress on the cell during the whole experimental procedure, avoid interference with the RBC's physiological processes, and offer precise control over its environment. Nevertheless, existing experimental approaches to RBC analysis specifically on the single-cell level include manipulations that often cause difficulties with preserving the RBC's integrity in a controlled microenvironment. These procedures include methanol fixation[23] or adsorbing the cells onto poly-lysine covered glass surfaces, which might lead to adsorption-dependent changes of the cell's intrinsic properties.[24] Alternative methods use active immobilization of single RBCs by optical tweezers in order to avoid adsorption-induced effects due to chemical fixation. However, the required high-intensity trapping lasers can already induce hemolysis,[10] and the stress levels introduced on the RBC often represent the limiting factor in acquiring information of which the experiment is actually aiming for.[18]

Here, we present a self-filling microfluidic device for single RBC assays starting directly with unprocessed, small volume human blood samples. Our method enables a noninvasive approach to single RBC experiments by using a specialized microfluidic geometry. In particular, our microfluidic design solely exploits the unique mechanical properties of the RBC itself in order to autonomously separate and isolate single red blood cells from the undiluted bulk into diffusion-controlled microchambers. The cells are confined horizontally within the chambers, representing ideal conditions for versatile microscopic and spectroscopic studies on single RBCs without any chemical fixation and its corresponding adsorption-induced effects. Furthermore, no active immobilization of individual RBCs by optical tweezers is required, which drastically reduces the accumulated photon dose on single functional RBCs during examination. Analysis of RBC flickering via bright-field microscopy or investigation of their oxygenation state using Raman microscopy is therefore not limited by photo-degradation introduced through high-intensity trapping lasers. Variation of the RBC's microenvironment through applying different buffer solutions is further precisely controlled by diffusion. This precise reaction control enables for an experimental time-resolved flickering analysis during the reversible shape evolution of non-adherent RBCs from the discocyte to the echinocyte morphology under altering osmolarity. Due to its unique combination of features, our specialized microfluidic device provides access to reversible, long-term, and time-resolved analysis of single RBCs under precise control of their environment.

MATERIALS AND METHODS

Design and operation of the blood chip

Polydimethylsiloxane (PDMS) is the most commonly used stamp resin for the fabrication of microfluidic devices, but its external surface is inherently hydrophobic[25] and can be only temporarily rendered hydrophilic by exposing the surface to an oxygen plasma.[26] Our microfluidic blood chip captures single RBCs directly from unprocessed, small volume human blood samples into specialized microchambers. The surface hydrophilicity of the PDMS replica is made more permanent through thermal aging[27] before oxygen plasma exposure in order to facilitate self-filling of the chip. Unprocessed blood can therefore be directly applied on the empty device and its filling is purely driven by capillarity (Fig. 1(a)).

Our specialized multi-height geometry exploits the unique mechanical properties of the RBC itself in order to separate individual RBCs from undiluted whole blood with a high cell volume fraction into a microenvironment without interactions with other cells. In particular, the

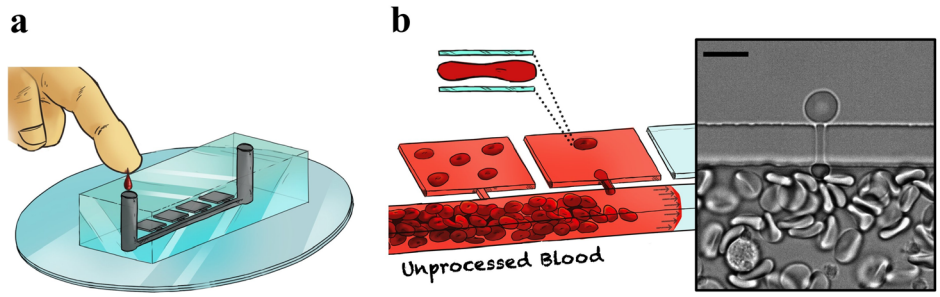

FIG. 1. Design and operation of the blood chip for noninvasive and versatile single RBC analysis. (a) Unprocessed human blood can be directly applied on the empty device and its initial filling is purely driven by capillarity. (b) Single RBCs are passively separated by capillary forces from the high cell density bulk through narrow connections between the controlling channel and low-height microchambers. Individual RBCs are further placed horizontally inside the chambers and are only confined with respect to motions out of the image plane, offering ideal conditions for versatile microscopic or spectroscopic studies on single functional RBCs. Scale bar: 10 μm.

dimensions of the connections (cross-section: $2 \times 2\,\mu m^2$ and length: $10\,\mu$m) between the controlling channel (width: $50\,\mu$m and height: $10\,\mu$m) and the microchambers (area: $100 \times 100\,\mu m^2$ and height: $2\,\mu$m) are in the size range of the smallest human capillaries to minimize the probability of RBCs entering the chambers. Consequently, as unprocessed blood is flowing through the initially empty device driven by capillary forces, separation as well as isolation of individual RBCs from the bulk into a single cell environment is achieved autonomously without any chemical or active physical manipulations. The unselective nature of this filling process with respect to the mechanical properties of the RBCs further excludes a potential bias of the subpopulation in the microchambers. Due to the low height of the chambers, the RBCs are placed horizontally inside them and are only confined with respect to motions out of the image plane, creating ideal conditions for versatile microscopic or spectroscopic studies on single functional RBCs (Fig. 1(b)).

After the initial filling of the device, washing of the controlling channel with buffers is actively regulated by advection. Due to the microfluidic nature of the blood chip, the flow in the controlling channel is laminar. Material transport into the filled microchambers and *vice versa* is now precisely controlled by diffusion, resulting from the multi-height design in addition to much smaller dimensions of the connecting channels compared to the controlling channel (Fig. 2(a)).[28–30] The concentration of an added or depleted biochemical reagent inside the flow-free chambers is therefore directly related to the diffusion time that has elapsed since the onset of an exchange buffer at the corresponding connecting channel. Variation of the RBC's microenvironment inside the flow-free chambers is further highly controlled and repeatable, e.g., by diffusive washing with different buffer solutions through the controlling channel

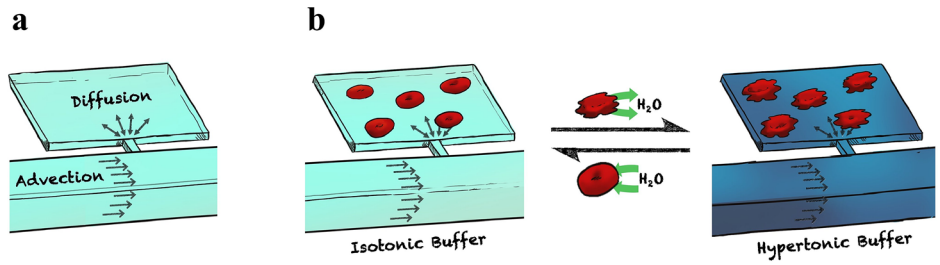

FIG. 2. Precise control over the microenvironment of confined single RBCs. (a) After initial filling of the device, flushing of the controlling channel is dominated by advection. The multi-height design in combination with much smaller dimensions of the connecting channels compared to the controlling channel results in diffusion-controlled material transport into flow-free microchambers and *vice versa*. (b) Precise and reversible control over the RBC's microenvironment enables the quantification of the temporal behavior of single RBCs exposed to an external stimulus, e.g., increasing the osmolarity by diffusive washing of the microchambers with hypertonic buffer through the controlling channel.

(Fig. 2(b)). As a result, our approach can serve as a general system to study the temporal behavior of single RBCs exposed to external stimuli.

Fabrication of the microfluidic device

Microfluidic devices were fabricated using soft lithography. In order to produce multi-height masters for further device fabrication, multi-layer photolithography was used to pattern the microfluidic design through a chrome mask (ML&C GmbH, Jena, Germany) on a silicon wafer (Si-Mat, Kaufering, Germany). Conventional photolithography using a MJB4 mask aligner (SUSS MicroTec AG, Garching, Germany) and SU8-2002 negative resist (MicroChem, Newton, MA, USA) as a first layer and SU8-3005 (MicroChem, Newton, MA, USA) as a second layer was applied to create microchambers and their connecting channels of 2 μm in height and a controlling channel with a height of 10 μm. Polydimetylsiloxane (PDMS) and cross-linker (Sylgard 184, Dow Corning GmbH, Wiesbaden, Germany) were mixed at 10:1 ratio and poured on the master, first degassed and cured at 80 °C for 24 h. Cured PDMS was peeled off from the master. Holes of the inlets were punched before the PDMS replica was placed onto a hotplate at 150 °C for 30 min for thermal aging in order to render its surface hydrophilicity, induced by the following exposure to oxygen plasma, more permanent. The PDMS replica was covalently bound to a glass slide after surface activation for 30 s in oxygen plasma (Harris Plasma, NY, USA) and the fabricated devices were left at room temperature for at least 12 h to a maximum of 36 h before use.

Blood sample collection and initial filling of the device

Human blood samples were freshly prepared before each experiment by finger pricking of a healthy donor and directly applied on the empty microfluidic device without any sample preparation.

Microscopy

An Olympus IX81 inverted microscope equipped with a 100× (N.A. 1.49) UApo N oil immersion objective (Olympus, Tokyo, Japan) was used for bright-field microscopy experiments. Images were recorded with a pco.edge camera (PCO AG, Kelheim, Germany) at 900 fps in the steady states as well as during the entire disco-echino-discocyte transitions.

Confocal Raman setup

Resonance Raman spectra were recorded using a custom-built confocal Raman microscopy setup. A 532 nm diode-pumped solid-state laser (SOLE laser system, Rodgau-Dudenhofen, Germany) was used for Raman excitation and was focused on the sample with a 100× (N.A. 1.4) PlanApo oil immersion objective (Olympus, Tokyo, Japan). The Stokes-shifted Raman signal was then collected into a 50 μm multimode optical fiber (Ocean Optics, Dunedin, FL, USA) acting as a pinhole and connected to a spectrometer (QE65 Pro-Raman, Ocean Optics, Dunedin, FL, USA).

Analysis of diffusive behavior and cell membrane edge fluctuations

Image processing algorithms using MATLAB were applied to identify the contour of the RBCs, determine the center of mass movement, and calculate the mean square displacement, $\mathrm{MSD} = \langle r(\tau)^2 \rangle = \langle (r(t+\tau) - r(t)) \rangle^2$, where τ is the time interval, from the corresponding trajectories. In two dimensions, the time dependence of the MSD can be described by: $\langle r(\tau) \rangle^2 = 4 \cdot M_\alpha \cdot \tau^\alpha$, where α is the scaling exponent and M_α the motility coefficient.[31] Motion is transported or super-diffusive for $\alpha > 1$, limited or sub-diffusive for $\alpha < 1$, and freely diffusing or random walk-like for $\alpha = 1$.[31,32]

In order to analyze the 1D-rotational motion of confined RBCs in the image plane in addition to the cell membrane edge fluctuations, the mean-centered Cartesian coordinates of the

RBC's contours were first converted into polar coordinates with the radius r at the angle β at equiangular distances of 0.5°. The polar coordinates were then partitioned into a Fourier function, $r(\beta,t) = c_0(t) + \sum_{q=1}^{n}[c_q(t) \cdot \cos(q \cdot \beta + \phi_j(t))]$, using multiple trigonometric regression. Here, $c_q(t)$ are the amplitudes of the harmonic q, which represent a set of $n = 360$ independent and uncorrelated shape descriptors and measure the amount of the frequency present in the contour of the cell. The zeroth harmonic describes a circle with the mean radius of the cell around its center of mass, the first harmonic the contribution of an offset circle, the second harmonic the amount of elongation, the third a trefoil, etc. The phase angles $\phi_q(t)$ of the harmonic q contain information about the best-fit rotation of the harmonic figure to a position of maximum correspondence with the observed boundary outline of the RBCs. The phase of the first noncircular Fourier frequency, $\phi_{q=2}(t)$, was used to estimate the amount of rotation exhibited by the RBCs. Global membrane edge fluctuations $\sqrt{\langle U^2 \rangle}$ were calculated from the Fourier harmonic amplitudes $c_q(t)$ by $\sqrt{\langle U^2 \rangle} = \sqrt{\sum_{q=0}^{n} \langle (c_q(t) - \langle c_q \rangle)^2 \rangle}$, using a series of 9×10^4 consecutive images in the steady states as well as during the disco-echino-discocyte transitions.

Diffusive washing of the chambers and calculation of osmolarity

Isotonic buffers for diffusive washing of the microchambers by flushing the controlling channel using appropriate tubing and syringe pumps (Cetoni GmbH, Germany) consisted of phosphate-buffered saline (PBS) with 1 mg/ml BSA and 10 mM glucose. Hypertonic buffers (1088 mOsm) contained additional 25 mg/ml NaCl. Polystyrene beads (1 μm diameter, Polysciences) were further added to the appropriate buffers during the disco-echino-discocyte transition in order to trace the onset of the exchange solutions at the connecting channel to the microchamber.

Material transport into the microchambers and *vice versa* is dominated by diffusion and the time t that has elapsed since the onset of the exchange buffers at the connecting channel to the microchamber was directly related to the NaCl concentration inside the chamber by $c(x,y,t) = \frac{c_0}{4\pi D t} e^{-(x^2+y^2)/4Dt}$. Here, x and y are the coordinates of the RBC's center of mass, c_0 is the concentration of the hypertonic buffer in the controlling channel, and $D = 1.473 \times 10^{-9}\,\mathrm{m^2\,s}$ is the diffusion coefficient of NaCl.[33] The osmolarity was then calculated by $\Pi(x,y,t) = \varphi \cdot n \cdot c(x,y,t)$, where $\varphi = 0.921$ is the osmotic coefficient of NaCl,[34] $n = 2$ the number of ions into which NaCl dissociates.

RESULTS AND DISCUSSION

Capturing efficiency of RBCs into the microchambers

In order to quantify the efficiency of the self-filling process, RBCs inside the microchambers were counted. The probability of chambers (area: $100 \times 100\,\mu\mathrm{m}^2$ and height: 2 μm) containing at least one RBC was 93.6% with a mean number of RBCs inside the filled chambers of $\langle N \rangle_{RBCs} = 19.8 \pm 10.6$. Considering that the mean volume of a RBC is about $\langle V \rangle_{RBCs} = 97\,\mathrm{fL}$,[35] the volume fraction of RBCs inside the chambers is $\chi = \langle N \rangle_{RBCs} \cdot \langle V \rangle_{RBCs} / V_{chamber} = (9.6 \pm 5.1)\,\%$, which is about one fourth to one fifth of the volume fraction of whole blood in the controlling channel. During the filling process, hemolysis of individual RBCs can occur, resulting in so-called RBC ghosts. However, the fraction of lysed RBCs inside the microchambers was only 4.8% with 53.3% of the chambers containing no ghosts. Furthermore, 97.6% of the microchambers showed no other type of blood cells than RBCs, with the remaining chambers containing a maximum of one other cell type.

RBC diffusive behavior and membrane edge fluctuations

Individual functional RBCs inside the microchambers are investigated by bright-field microscopy (Fig. 3(a), Video: supplementary material). Although being confined with respect to

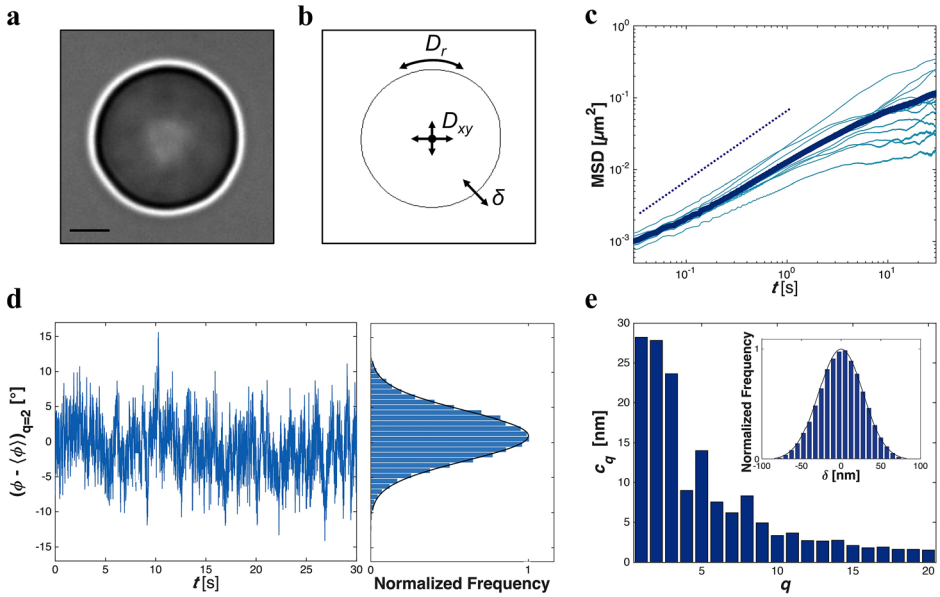

FIG. 3. Diffusive behavior and cell edge fluctuations of functional RBCs inside the microchambers. (a) Bright-field microscopy image of a typical RBC inside a microchamber, confined with respect to movement out of the image plane. Scale bar: 2 μm. (b) The specialized geometry of the microfluidic chambers conserves the RBC's 2D-translational motion in the image plane (D_{xy}) and around the z-Axis (D_r) in addition to their membrane edge fluctuations (δ). (c) Mean square displacement calculated from the center of mass of single RBCs inside microchambers under unprocessed blood conditions clearly indicates that their motility is diffusive with an absence of adhesive interaction. (d) Typical time record and the deviation from the mean value of the phase angle of the second Fourier harmonic shows that the rotational motion of RBCs in the image plane is also random walk-like. (e) Typical time-averaged amplitude spectrum and summation over all harmonics of the deviation δ (inset) from their corresponding time average for the first 20 harmonics of a RBC inside a microchamber.

movements out of the image plane, the cells are still exhibiting 2D-translational (D_{xy}) and 1D-rotational motion around the z-axis (D_r) in addition to membrane edge fluctuations (δ) (Fig. 3(b)). The mean square displacement (MSD), calculated from the center of mass movement of single RBCs under unprocessed blood conditions (Fig. 3(c)), shows the absence of adhesive interactions. In particular, the mean slope of $\alpha \approx 1$ indicates that their motility inside the microchambers is diffusive with a translational diffusion constant of $D_{xy} = (4.3 \pm 2.4) \times 10^{-3}\,\mu\text{m}^2/\text{s}$.

Fourier analysis is a commonly applied method for particle shape characterization[36] and the phase of the first non-circular Fourier frequency, $\phi_{q=2}(t)$, can be used to estimate the amount of rotation exhibited by a moving object. The trajectory and its deviation from the mean value of $\phi_{q=2}(t)$ for a single RBC inside a chamber (Fig. 3(d)) indicate that the rotational motion in the image plane is also diffusive with a rotational diffusion constant of $D_r = (1.1 \pm 0.8) \times 10^{-2}\,\text{rad}^2/\text{s}$. Consequently, the analysis of the global membrane edge fluctuations is based on a translationally and rotationally invariant description using their Fourier harmonic amplitudes $c_q(t)$. The time-averaged amplitude spectrum for the first 20 harmonics of a typical single RBC inside a microchamber is shown in Fig. 3(e). Summation over all harmonics of the deviation from the time average, $\delta = \sum_{q=0}^{n}(c_q(t) - \langle c_q \rangle)$, leads to the corresponding fluctuation histogram (Fig. 3(e), inset). Fluctuations of the membrane global edge $\sqrt{\langle U^2 \rangle}$ are determined from the harmonic amplitudes by $\sqrt{\langle U^2 \rangle} = \sqrt{\sum_{q=0}^{n}\langle (c_q(t) - \langle c_q \rangle)^2 \rangle}$. The first fluctuation mode, $\langle U_{q=1}^2 \rangle$, can be further related to the bending modulus $\kappa = 6 \cdot 10^{-3} k_B T R^2 / \langle U_{q=1}^2 \rangle$, where R is the cell radius.[7] Under initial unprocessed blood conditions, we obtain $\sqrt{\langle U^2 \rangle}_{blood} = (21.9 \pm 1.8)\,\text{nm}$ and $\kappa_{blood} = (7.1 \pm 1.3) \times 10^{-19}\,\text{J}$. After diffusive washing of the chambers by flushing the controlling channel with isotonic phosphate-buffered saline (PBS), the RBCs retained their motility and the membrane edge fluctuations of the same RBC population

changed marginally. Under these conditions, $\sqrt{\langle U^2 \rangle}_{buffer} = (21.1 \pm 2.1)\,\text{nm}$ and $\kappa_{buffer} = (7.4 \pm 1.6) \times 10^{-19}\,\text{J}$, which are in good agreement with values of $\sqrt{\langle U^2 \rangle}_{buffer}$ and κ_{buffer} reported in the literature.[7–9]

Reversible RBC oxygenation cycle by confocal resonance Raman spectroscopy

The horizontal confinement of single RBCs in flow-free microchambers offers an optimal environment not only to investigate the mechanical properties of the membrane but also to further apply advanced optical methods in order to study molecular processes within the red blood cell. Raman microscopy is suited especially to investigate RBCs, due to absorption of visible light by the porphyrin groups in hemoglobin (Hb). If the Raman excitation wavelength matches a transition wavelength of the molecule, a selective resonance enhancement of the porphyrin Raman signal occurs, without spectral interference from the surrounding protein.[37,38]

A process within RBCs that is well-known to be sensitive to photo-dissociation is the binding of oxygen to Hb.[39] The Raman bands at $1640\,\text{cm}^{-1}$, $1582\,\text{cm}^{-1}$, and $1378\,\text{cm}^{-1}$ are characteristic for the oxygenated form of human hemoglobin (oxyHb) and undergo a shift to $1604\,\text{cm}^{-1}$, $1553\,\text{cm}^{-1}$, and $1355\,\text{cm}^{-1}$ upon transition to the deoxygenated form (deoxyHb). Furthermore, using high laser intensities leads to a photo-induced conversion of oxyHb (Fe^{2+}) to the inactive metHb (Fe^{3+}) state, where the oxygen is irreversibly bound to the heme group.[18]

We used a custom-built confocal Raman setup to investigate the photo-induced oxygenation cycle of single RBCs confined inside microchambers. Without the necessity of high-intensity optical tweezers for cell immobilization, our approach drastically reduces the accumulated photon dose on the RBC. Resonance Raman spectra of single functional RBCs with Hb solely in the oxygenated state were recorded by choosing the power of the Raman excitation laser ($\lambda = 532\,\text{nm}$) to be merely $1\,\mu\text{W}$ before entering the microscope objective (Fig. 4(a), bottom). Increasing the laser power to $80\,\mu\text{W}$ already leads to a mixture between the oxygenated and deoxygenated Hb states within the cells (Fig. 4(a), middle), whereas applying $400\,\mu\text{W}$ results in complete photo-induced conversion to deoxyHb (Fig. 4(a), top). Due to constant diffusive washing of the microchambers with fresh isotonic buffer via the controlling channel, the photo-dissociation is reversible when the excitation power is again decreased to $1\,\mu\text{W}$.

In order to further investigate the photo-induced deoxygenation process, we determined the background-corrected and normalized intensity ratio $I_{1582\,\text{cm}^{-1}}/I_{1553\,\text{cm}^{-1}}$ for various excitation

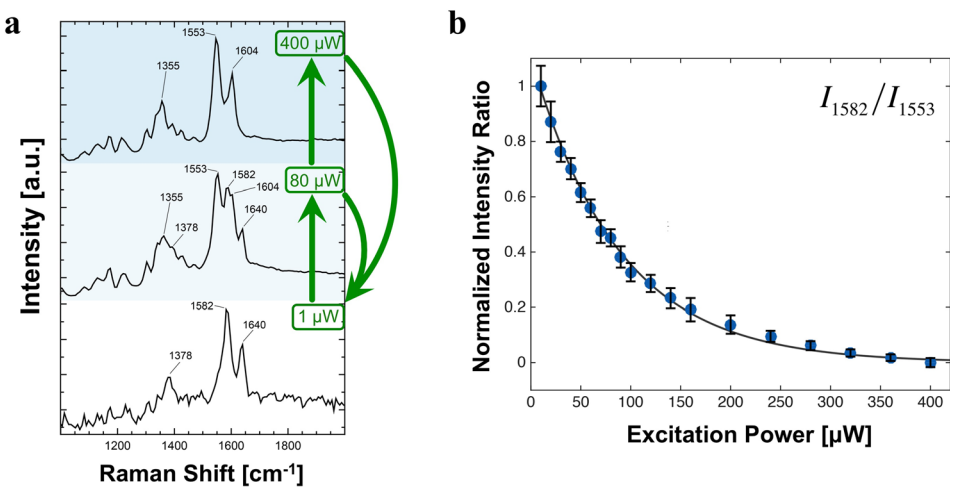

FIG. 4. Resonance Raman spectroscopy of the reversible, photo-induced oxygenation cycle of single functional RBCs confined in microchambers. (a) Typical resonance Raman spectra of a RBC inside a microchamber showing the change of the characteristic bands during the reversible photo-dissociation of oxygen from Hb. Integration time for each spectrum: 10 s. (b) Background-corrected and normalized intensity ratio between the most prominent oxyHb ($1582\,\text{cm}^{-1}$) and deoxyHb ($1553\,\text{cm}^{-1}$) Raman bands as a function of increasing laser power during the photo-induced dissociation process of oxygen from Hb inside confined RBCs.

powers (Fig. 4(b)), showing that already a slight increase in laser intensity leads to a significant conversion of oxyHb to deoxyHb inside the RBCs with a critical excitation power of $P_{crit} = (88.3 \pm 3.7)\ \mu$W.

Time-resolved characterization of the reversible RBC shape evolution under altering osmolarity

When not subjected to external stress and under physiological conditions, normal human RBCs assume a distinctive biconcave discoid morphology, the well-known discocyte. However, it has been known for more than half a century that RBCs exist in a variety of shapes under certain conditions.[40] For instance, increasing salt concentration leads to the morphological transition from the discocyte to a series of crenated echinocyte shapes,[41] which do not depend on the echinocytogenic agent.[14]

The blood chip enabled the time-resolved experimental tracking and membrane fluctuation analysis of non-adherent RBCs during the reversible shape evolution from the discocyte to the echinocyte morphology. The analysis of the reversible disco-echinocyte transition of a typical RBC is shown in Fig. 5(a) (Video, supplementary material). First, the device was washed with isotonic buffer via the controlling channel after its' self-filling with unprocessed blood and a discocyte-shaped RBC inside one of the microchambers as selected for fast bright-field imaging. Subsequently, the osmolarity Π was increased by diffusive washing of the microchamber through flushing the controlling channel with hypertonic buffer ($\Pi = 1088$ mOsm), containing polystyrene (PS) beads in order to precisely trace its arrival at the connecting channel. After the disco-echinocyte transition of the RBC was completed, the device was washed with an identical hypertonic solution lacking PS beads. Finally, the microchamber was again washed diffusively by flushing the controlling channel with isotonic buffer including PS beads to initiate and trace the transition of the RBC back to the discocyte morphology. Before and after each diffusive washing period, the steady states of the RBC were recorded and resulted in the corresponding membrane edge fluctuation amplitudes (Fig. 5(a), blue points). Material transport into the microchambers and *vice versa* is precisely controlled by diffusion and the time that elapsed since the traced onset of the buffers at the connecting channel is therefore directly related to the osmolarity at the position of the RBC inside the chamber. Consequently, measuring the RBC's membrane edge fluctuations inside the chambers is not limited to steady states and $\sqrt{\langle U^2 \rangle}$ can be analyzed dynamically on the single cell level during the whole disco-echino-discocyte transition (Fig. 5(a), blue lines, Video, supplementary material).

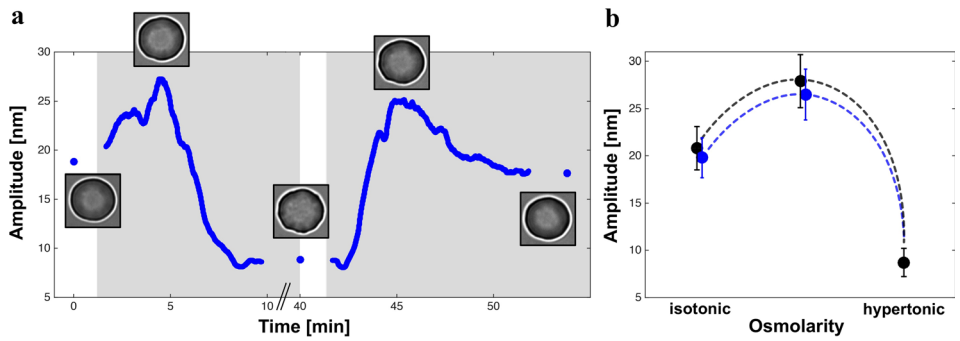

FIG. 5. RBC's membrane edge fluctuation analysis of the reversible shape evolution under altering osmolarity. (a) Reversible transition of a typical RBC from the discocyte to the echinocyte morphology with the corresponding membrane edge fluctuations as a function of time after the arrival of the exchange buffers. Bright-field images of intermediate morphologies during the transition are shown at maximum amplitudes as well as at isotonic and hypertonic steady states. (b) Membrane edge fluctuation analysis of functional RBCs during reversible disco-echinocyte transformations under altering osmolarity. Black symbols and lines (guides to the eye) indicate the evolution of the membrane fluctuations from the initial isotonic steady states via the intermediate shapes with maximum amplitudes to the final hypertonic steady states, whereas blue symbols and lines (guides to the eye) indicate the reversible process back to the restored biconcave shapes under isotonic conditions.

The membrane edge fluctuation analysis during the reversible shape evolution of individual RBCs inside microchambers is shown in Fig. 5(b). In the initial isotonic steady state, the membrane fluctuation amplitude of discocyte RBCs is $\sqrt{\langle U^2\rangle}_{iso,\,initial} = (20.8 \pm 2.3)\,\text{nm}$ and the arrival of the hypertonic buffer at the connecting channel to the microchamber induces the disco-echinocyte transitions. During the shape transformation, the membrane edge fluctuations first increase substantially to a maximum of $\sqrt{\langle U^2\rangle}_{max,\,iso\rightarrow hyper} = (27.9 \pm 2.8)\,\text{nm}$ at intermediate morphologies, before largely decreasing to $\sqrt{\langle U^2\rangle}_{hyper} = (8.7 \pm 1.5)\,\text{nm}$ for the final echinocytes in the hypertonic steady state. The rise in membrane fluctuation amplitude for intermediate morphologies during the disco-echinocyte transformation is most likely due to a small decrease in membrane tension accompanying the modest reduction in cell volume during the early stages of the transition. However, the steep rise in hemoglobin concentration eventually leads to the suppression of the membrane fluctuations in the final echinocyte shape, effects that also have been observed in measurements limited to the steady states of RBCs exposed to hypertonic buffers.[8] Diffusive washing of the microchamber with isotonic buffer starts the transition back to the discocyte. Fluctuations of the membrane again increase to a maximum of $\sqrt{\langle U^2\rangle}_{max,\,hyper\rightarrow iso} = (26.5 \pm 2.7)\,\text{nm}$, before reaching the restored isotonic steady state with $\sqrt{\langle U^2\rangle}_{iso,\,restored} = (19.8 \pm 2.1)\,\text{nm}$. The bright-field optical images of the restored isotonic discocyte morphologies and the marginal difference of $\sqrt{\langle U^2\rangle}_{iso,\,restored}$ compared to the initial isotonic state indicate that the disco-echino-discocyte transition is largely reversible.

One of the fundamental questions regarding RBCs that still remains controversial is whether the fluctuations of the membrane are driven by an active process or are simply thermal motion.[10] Using our specialized device, the time-resolved analysis of a single RBC's morphological response with its related alterations of the membrane edge fluctuation amplitude shows a timescale of about 10 min. This is significantly slower than the change in osmolarity at the RBC's position inside the microchamber via diffusive washing. In particular, the grey areas in Fig. 5(a) correspond to the time when already more than 90% of excess NaCl diffused from the controlling channel to the position of the RBC inside the microchamber ($\Pi(t) > 1009\,\text{mOsm}$, isotonic $\rightarrow$ hypertonic) and *vice versa* ($\Pi(t) < 379\,\text{mOsm}$, hypertonic $\rightarrow$ isotonic), i.e., when the osmolarity inside the chamber already reached a steady state. Water transport across the membrane of human RBCs is extremely fast, changing the cell's water content in a time-scale of about 20 ms at room temperature.[42] Therefore, RBC membrane permeability to water as a limiting factor is unlikely to explain the observed time delay of the morphological response and its corresponding alterations in fluctuation amplitude to changes in osmolarity, which might support studies suggesting active membrane processes contributing to RBC flickering.[9,10,43]

CONCLUSIONS

We introduced a straightforward, self-filling microfluidic device that enables noninvasive, controlled and versatile single RBC experiments, starting directly with unprocessed human blood samples. Existing approaches to red blood cell studies typically require pre-experimental sample preparation and the principle that allows investigations specifically on the single cell level is often either based on a form of chemical fixation or active immobilization by high-intensity optical tweezers. In contrast, our method autonomously separates and isolates individual RBCs directly from the unprocessed, high cell density bulk and confines them horizontally in diffusion-controlled microchambers by solely exploiting their unique mechanical properties. The noninvasive, horizontal confinement in combination with a precise control over the RBC's microenvironment represents ideal conditions for various microscopic or spectroscopic investigations in order to quantify the temporal behavior of single RBCs exposed to an added or depleted biochemical reagent.

Inside the microchambers, the motility of the RBCs is diffusive and they are therefore not experiencing adsorption-dependent changes of their intrinsic properties that can occur using chemical fixation.[24] The confinement is also passive in the sense that no active immobilization

by optical tweezers is needed, eliminating corresponding photo-degradation or spurious photo-induced effects that inherently prohibit the access to reversible or long-term experiments on single functional RBCs. The accumulated radiation dose introduced through high-intensity trapping lasers can lead to hemolysis of RBCs[10] or induces the conversion of oxyHb to the inactive metHb state,[18] both limiting the information that can be acquired by either microscopic or spectroscopic techniques. Our approach overcomes this limitation and combined with confocal resonance Raman spectroscopy we were able to record Raman spectra of functional individual RBCs purely in the oxyHb state. We showed that the laser power that is sufficient to already induce a conversion of oxyHb to deoxyHb inside the cell is in the μW range, which is only a fraction of what is typically applied in optical tweezers based methods. Due to the precise control over the RBC's environment inside the microchambers, analysis of RBC flickering is additionally not limited to steady states. In particular, the dynamic measurement of non-adherent RBC's morphological response to increasing osmolarity became feasible. The time-resolved analysis of membrane edge fluctuations reveals a time delay in shape transformation of the RBC with respect to changes in osmotic concentrations. In summary, our specialized microfluidic device offers a unique combination of features that opens new possibilities for reversible, long-term, and time-resolved analysis of RBCs on the single-cell level. Overcoming the limitations of available approaches, our method will enable studies investigating the temporal behavior of single RBCs under precise control of their environment. Time-resolved analysis of single RBCs exposed to external stimuli will provide important insights into their fundamental biophysical properties like flickering of the membrane[10] as well as biomedical questions regarding the disease progression in malaria[12] or *in-vitro* aging of RBCs during storage in blood banks.[44]

SUPPLEMENTARY MATERIAL

See supplementary material for Video 1: Bright-field microscopy video (real-time) of a typical RBC inside a microchamber in unprocessed blood conditions. Video 2: Bright-field microscopy video (10× faster) of the disco-echinocyte transformation of a typical RBC after arrival of the hypertonic exchange buffer at the connection to the microchamber at $t = 00:00$ min. Video 3: Bright-field microscopy video (10× faster) of the echino-discocyte transformation of a typical RBC after arrival of the isotonic exchange buffer at the connection to the microchamber at $t = 00:00$ min.

ACKNOWLEDGMENTS

Financial support by the Swiss National Science Foundation (SNF_ 200020_141270) is gratefully acknowledged. A.C.T. thanks the "Forschungsfond der Universität Basel" (DCH2106) for its support.

[1]N. Mohandas and P. G. Gallagher, Blood **112**, 3939–3948 (2008).
[2]J. Rey, P. A. Buffet, L. Ciceron, G. Milon, O. Mercereau-Puijalon, and I. Safeukui, Sci. Rep. **4**, 3767 (2014).
[3]J. R. Heath, A. Ribas, and P. S. Mischel, Nat. Rev. Drug Discovery **15**, 204 (2015).
[4]J. C. A. Cluitmans, V. Chokkalingam, A. M. Janssen, R. Brock, W. T. S. Huck, and G. J. C. G. M. Bosman, Biomed Res. Int. **2014**, 1–9.
[5]T. Browicz, Zbl. Med. Wissen **28**, 625–627 (1890).
[6]F. Brochard and J. F. Lennon, J. Phys. **36**, 1035–1047 (1975).
[7]H. Strey, M. Peterson, and E. Sackmann, Biophys. J. 1995, **69**, 478–488.
[8]J. Evans, W. Gratzer, N. Mohandas, K. Parker, and J. Sleep, Biophys. J. **94**, 4134–4144 (2008).
[9]T. Betz, M. Lenz, J.-F. Joanny, and C. Sykes, Proc. Natl. Acad. Sci. U.S.A. **106**, 15320–15325 (2009).
[10]H. Turlier, D. A. Fedosov, B. Audoly, T. Auth, N. S. Gov, C. Sykes, J.-F. Joanny, G. Gompper, and T. Betz, Nat. Phys. **12**, 513 (2016).
[11]C. Wagner, P. Steffen, and S. Svetina, C. R. Phys. **14**, 459–469 (2013).
[12]D. Cojoc, S. Finaurini, P. Livshits, E. Gur, A. Shapira, V. Mico, and Z. Zalevsky, Biomed. Opt. Express **3**, 991 (2012).
[13]P. Abbyad, P.-L. Tharaux, J.-L. Martin, C. N. Baroud, and A. Alexandrou, Lab Chip **10**, 2505–2512 (2010).
[14]H. W. G. Lim, M. Wortis, and R. Mukhopadhyay, Proc. Natl. Acad. Sci. U.S.A. **99**, 16766–16769 (2002).
[15]K. A. Melzak, G. R. Lázaro, A. Hernández-Machado, I. Pagonabarraga, J. M. Cárdenas Díaz de Espada, and J. L. Toca-Herrera, Soft Matter **8**, 7716 (2012).
[16]G. R. Lázaro, K. A. Melzak, J. L. Toca-Herrera, I. Pagonabarraga, and A. Hernández-Machado, Soft Matter **9**, 6430 (2013).
[17]C. Xie and Y. Q. Li, J. Appl. Phys. **93**, 2982–2986 (2003).

[18]K. Ramser, J. Enger, M. Goksör, D. Hanstorp, K. Logg, and M. Käll, Lab Chip **5**, 431–436 (2005).
[19]B. R. Wood, P. Caspers, G. J. Puppels, S. Pandiancherri, and D. McNaughton, Anal. Bioanal. Chem. **387**, 1691–1703 (2007).
[20]A. C. De Luca, G. Rusciano, R. Ciancia, V. Martinelli, G. Pesce, B. Rotoli, L. Selvaggi, and A. Sasso, Opt. Express **16**, 7943–7957 (2008).
[21]G. Rusciano, G. Pesce, and A. Sasso, Haematologica **92**, 174–183 (2007).
[22]G. Rusciano, A. C. De Luca, G. Pesce, and A. Sasso, Sensors **8**, 7818–7832 (2008).
[23]C. W. Ong, Z. X. Shen, K. K. H. Ang, U. A. K. Kara, and S. H. Tang, Appl. Spectrosc. **53**, 1097–1101 (1999).
[24]K. Ramser, E. J. Bjerneld, C. Fant, and M. Käll, J. Biomed. Opt. **8**, 173–178 (2003).
[25]J. C. Mcdonald, D. C. Duffy, J. R. Anderson, and D. T. Chiu, Electrophoresis **21**, 27–40 (2000).
[26]B.-H. Jo, L. M. Van Lerberghe, K. M. Motsegood, and D. J. Beebe, J. Microelectromech. Syst. **9**, 76–81 (2000).
[27]D. T. Eddington, J. P. Puccinelli, and D. J. Beebe, Sens. Actuators, B **114**, 170–172 (2006).
[28]S. Deshpande and T. Pfohl, Biomicrofluidics **6**, 034120 (2012).
[29]S. Deshpande and T. Pfohl, PLoS ONE **10**, e0116521 (2015).
[30]A. Hochstetter, E. Stellamanns, S. Deshpande, S. Uppaluri, M. Engstler, and T. Pfohl, Lab Chip **15**, 1961–1968 (2015).
[31]S. Uppaluri, J. Nagler, E. Stellamanns, N. Heddergott, S. Herminghaus, M. Engstler, and T. Pfohl, PLoS Comput. Biol. **7**, e1002058 (2011).
[32]Y. Han, A. M. Alsayed, M. Nobili, J. Zhang, T. C. Lubensky, and A. G. Yodh, Science **314**, 626–630 (2006).
[33]V. Vitagliano and P. A. Lyons, J. Am. Chem. Soc. **78**, 1549–1552 (1956).
[34]W. J. Hamer and Y. Wu, J. Phys. Chem. Ref. Data **1**, 1044–1099 (1972).
[35]C. E. McLaren, G. M. Brittenham, and V. Hasselblad, Am. J. Physiol. **252**, H857–H866 (1987).
[36]B. W. Robert Ehrlich, SEPM J. Sediment. Res. **40**, 205–212 (1970).
[37]T. C. Strekas and T. G. Spiro, Biochim. Biophys. Acta-Protein Struct. **263**, 830–833 (1972).
[38]H. Brunner and H. Sussner, Biochim. Biophys. Acta-Protein Struct. **310**, 20–31 (1973).
[39]B. R. Wood and D. McNaughton, Biopolymers **67**, 259–262 (2002).
[40]E. Ponder, *Hemolysis and Related Phenomena* (Grune & Stratton, New York, 1948).
[41]M. Bessis and R. I. Weed, *Living Blood Cells and Their Ultrastructure* (Springer, New York, 1973).
[42]E. Gianolio, G. Ferrauto, E. Di Gregorio, and S. Aime, Biochim. Biophys. Acta-Biomembr. **1858**, 627–631 (2016).
[43]S. Tuvia, A. Almagor, A. Bitler, S. Levin, R. Korenstein, and S. Yedgar, Proc. Natl. Acad. Sci. U.S.A. **94**, 5045–5049 (1997).
[44]A. D'Alessandro, A. G. Kriebardis, S. Rinalducci, M. H. Antonelou, K. C. Hansen, I. S. Papassideri, and L. Zolla, Transfusion **55**, 205–219 (2015).